Rotational Disorder in Poly(*p*-phenylene terephthalamide) Fibers by X-ray Diffraction with a 100 nm Beam

S. Roth,[†] M. Burghammer,[†] A. Janotta,[‡] and C. Riekel*,[†]

European Synchrotron Radiation Facility, B.P. 220, F-38043 Grenoble Cedex, France, and Walter Schottky Institut, Am Coulombwall, 85748 Garching, Germany

Received September 23, 2002; Revised Manuscript Received December 3, 2002

ABSTRACT: Single fibers of poly(*p*-phenylene terephthalamide) (PPTA; brand names Kevlar^x, where x = 29, 49, 149) have been scanned with an about 100 nm synchrotron radiation X-ray beam normal to the fiber axis. Models of rotational disorder of the crystalline domains are discussed based on Monte Carlo simulations of the spatial variation of the 110/200 reflection intensities. For Kevlar^{149} the principal disorder appears to be a rotational domain-disorder across the fiber. The data suggest also the presence of a core and possibly a skin layer, which are both more disordered. Kevlar^{29,49} appear to have the same type of layering but with different volume fractions. There is also some evidence for a volume fraction without rotational correlation, which might be related to a morphology formed at the onset of coagulation.

Introduction

Poly(*p*-phenylene terephthalamide) (PPTA, brand names: Kevlar, Twaron) is one of the best studied cases of a high strength and high modulus polymer fiber.[1−3] It is therefore a well-suited model system to test advances in analytical techniques for investigating the microstructure of such fibers. Transmission electron microscopy/diffraction (TEM/TED) techniques are restricted to probing thin fiber sections and an extrapolation to a whole fiber is complicated by the sectioning process.[4−8] Scanning probe techniques, like atomic force microscopy (AFM), are surface sensitive and do not provide a complete information.[9−13] With the advent of third-generation synchrotron radiation (SR) sources, complementary scanning micro-X-ray diffraction (μ-XRD) experiments on single polymeric fibers have become possible.[14−16] Thus, μ-XRD experiments with a 3 μm diameter beam have demonstrated a gradient in orientation distribution in an about 12 μm diameter Kevlar^{29} fiber which disappears upon tensile deformation.[15] This suggests inhomogeneities in the orientation distribution of crystalline domains appearing in the course of the coagulation process and the processing of the fiber. These processes are assumed to result in a radially organized hydrogen-bonded fibrillar system.[17−20] μ-XRD data agree with this model but also show that the crystalline domains retain some disorder.[14−16] It is at present not understood in detail how order is improved during processing. This issue is addressed in the current article by probing the variation of disorder with μ-XRD in the series Kevlar^x (x: 29, 49, 149). We will also demonstrate in this article that X-ray beams of about 100 nm size are now available for probing polymer fibers. This allows addressing issues like skin/core differentiation in more detail than previously possible with micrometer-sized X-ray beams.

Experimental Section

Materials. Kevlar^x fibers (x = 29, 49, 149) were obtained from K. Gardner (DuPont). An increase in Young's modulus and therefore lattice perfection is obtained in the series Kevlar^{29} → Kevlar^{49} → Kevlar^{149} by a proprietary process involving heat treatment and uniaxial stress.[1] Mechanical properties and μ-XRD data with a 3 μm beam of this specific batch obtained at the European Synchrotron Radiation Facility (ESRF) have been reported elsewhere.[15] Single fibers were selected under a microscope and a few mm piece of fiber cut by microscissors. Each piece of fiber was glued to a washer, which was fixed on a brass pin so that the fiber axis was approximately horizontally oriented. The fiber axis was then optically aligned using a two-axis goniometer (Huber).

Synchrotron Radiation Experiments. μ-XRD experiments were performed at the ESRF microfocus beamline (ID13).[16] The photon beam from an undulator was monochromatized by a Si-111 double crystal to λ = 0.0975 nm. For further beam definition in the vertical plane an X-ray waveguide was used which provides a beam of ≈100 nm diameter at its exit.[21,22] Experiments were performed with the TE_0 mode.[21] The beam was focused in the horizontal direction to about 4 μm at the exit of the waveguide by a multilayer mirror.[22] The size and orientation of the waveguide beam on a scanning electron microscopy (SEM) picture of a Kevlar^{49} fiber is shown schematically in Figure 1A. The fiber axis was aligned normal to the waveguide horizontal axis with a precision of ±2°.

The scanning setup has been described in detail elsewhere.[22] Sample observation is possible in the horizontal and vertical directions by optical microscopes. A motorized gantry allows translating the sample between the microscopes and the beam at the exit of the waveguide with micrometer-repeatability. The position of the beam in the horizontal and vertical planes and the distance to the focal point of the horizontal microscope was determined by a calibration fiber-cross to about 1 μm precision. For high-resolution scans a piezo-module with 80 μm travel range and 0.1 μm repeatability along three orthogonal axes was used (TRITOR-module by Piezo-Jena). The fiber was positioned with the help of the vertical microscope at 50−100 μm from the waveguide exit. Given a divergence of the TE_0 mode of about 1 mrad, this implies that the vertical beam size at the sample position cannot be larger than 200 nm.[21,23]

A sequence of frames (diffraction patterns) was recorded while scanning the fiber in vertical direction through the beam with a step increment of 200 nm. At every position a 30-sec frame was recorded with a MAR−CCD detector. Calibration of detector center and distance-to-sample was done by a Ag−behenate standard.[24] The equatorial 110/200 reflections were fitted by two-dimensional Gaussian functions and a zero-order polynomial using the FIT2D program.[25] The fit to the experimental data for Kevlar^{49} and the difference pattern are shown in Figure 1B−D.

* Corresponding author.
[†] European Synchrotron Radiation Facility.
[‡] Walter Schottky Institut.

10.1021/ma021514g CCC: $25.00
Published on Web 02/07/2003

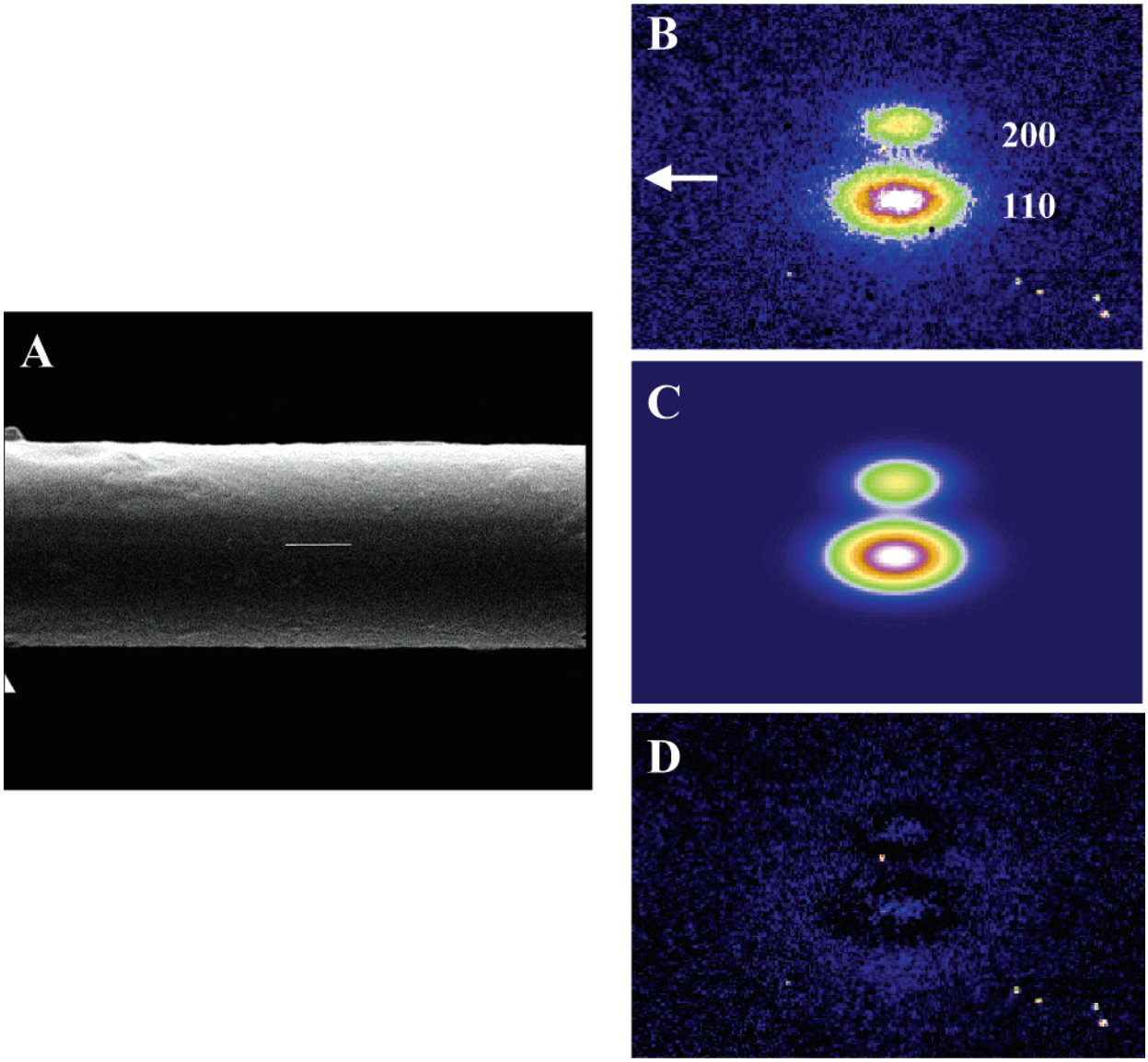

Figure 1. (A) SEM picture of Kevlar[49] fiber. The white line shows schematically the shape and orientation of the waveguide beam which has a dimension of about $0.1 \times 4\ \mu m^2$ at the waveguide exit. (B) Equatorial scattering of the Kevlar[49] fiber. An arrow indicates the meridional direction; $d_{110} = 0.434$ nm, $d_{200} = 0.390$ nm. (C) Simulated scattering by assuming 2D-Gaussian functions for the Bragg reflections and a 0-order 2D-polynomial for the background. (D) Difference pattern of parts A and B. All patterns are on the same scale.

Modeling

Structural models were based on the Northolt allomorph.[26] According to this structure the polymer chains are interconnected by hydrogen bonds to sheets, which are oriented parallel to the *b* axis. As indicated in the Introduction, the sheets and therefore the crystalline domains are aligned in radial direction, normal to the fiber axis. The crystalline domains, which form an ordered fibrillar structure, correspond to the basic load-bearing element of the macroscopic fiber. Crystalline domain sizes normal to the fiber axis derived from XRD and TEM/TED experiments are in the range 3−13 nm depending on the fiber perfection and the analytical method used.[17,27,28] The size of the waveguide X-ray beam is, however, at least a factor of 10 times larger than the domain size. The orientation of the hydrogen-bonded sheets is therefore averaged over all unit cells sampled by the beam. Crystallite sizes and spatial extent of the beam along the fiber axis will be neglected as only equatorial reflections are analyzed.

The idealized sheet model assumes that the hydrogen-bonded sheets are perfectly aligned on all hierarchical levels along the radial (*b* axis[29]) direction of the fiber (Figure 2A) which can be explained by the presence of strong tie bundles[4] between the domains. An alternative model (Figure 2B), based on a fully random rotational orientation of the domains throughout the fiber is discarded at this stage based on the previous results.[17−20] One cannot, however, exclude that the fibrils and hence crystalline domains have some rotational freedom around the fiber axis. It should also be noted that a skin/core differentiation and mixtures of more or less oriented domains have been reported based on SEM/TEM[4−6] and near field techniques.[30,31]

Analytical Simulations. For the idealized sheets model the (200) and (110) lattice planes are diffracting only for specific angles relative to the incoming beam corresponding to the Bragg condition.[14,16] These angles are symbolized in Figure 3A by arrows. The corresponding unit cell orientations with the *b* axes pointing along

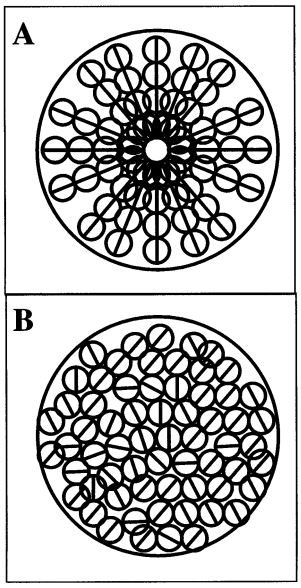

Figure 2. Model of rotational order in Kevlar based on domains projected on the fiber axis. Circles schematically depict crystalline domains, which are assumed to be smaller than the beam size. The solid lines correspond to the average orientation of hydrogen-bonded planes across each domain (see text): (A) radially correlated rotational orientation of domains; (B) uncorrelated orientation of domains.

the radial direction are shown for two of the arrows. The thinner arrows are generated due to the fiber symmetry. The analytical model assumes that the scattering probability of an equatorial reflection is proportional to the length of the arrow piece (l) covered by the beam.[14] l varies as the beam progresses through the sample during a scan. The relative reflection intensity is derived at every scan point by

$$I_{hk0} = lF^2_{hk0}PLG \tag{1}$$

where F_{hk0} is the structure factor and PLG are correction factors which depend on the X-ray source polarization and the experimental geometry.[32] Such simulations provide a qualitative agreement with scanning μ-XRD experiments.[14]

A more realistic analytical model assumes a rotational disorder of the individual domains as discussed above. On the basis of different degrees of domain interactions, two limiting models of rotational disorder can be defined.

(1) The first is M1: weak domain interactions resulting in a weak rotational correlation of domains across the fiber.[16] Given the decrease in Herman's orientation function from the skin to the core for the least ordered Kevlar[29] (see below and ref 15) a linear increase in rotational disorder of the domains toward the center will be assumed.

(2) The second is M2: strong domain interactions resulting in a correlated rotational disorder of domains. In this case, the rotational disorder is assumed to be constant across the fiber radius.

These models, which enlarge the Bragg condition across the fiber, are shown for the (110) reflection in Figure 3B,C. The assumption for modeling is that the rotational disorder-distribution of domains can be modeled by a Gaussian function with sigma-value σ_ϕ (angular variance). The Bragg condition will then be smeared out normal to the arrows and can be simulated by a Gaussian function with sigma-value σ_r (spatial variance). The M1 model assumes a constant value of σ_r along the fiber radius r, which corresponds to an increase in σ_ϕ from the skin to the core (Figure 3B). This is justified at least for Kevlar[29] in view of a gradient in orientation distribution[15] which implies that the fibrils are only loosely correlated. The local σ_r value is related to the angular σ_ϕ value via

$$\sigma_r = 2\tan(\sigma_\phi/2)r \tag{2}$$

In contrast, the M2 model assumes that the σ_ϕ value is constant across the fiber. Consequently the σ_r value depends on the radial position (Figure 3C). This implies a correlated rotational domain disorder which could be introduced by tie bundles between adjacent domains (fibrils).[4]

A value of about $\sigma_\phi = 420$ mrad was derived experimentally by recording a diffraction pattern with the microbeam oriented parallel to the fiber axis of a short piece of Kevlar[49].[33] Analytical simulations based on the M1 model for a Kevlar[49] fiber provide a semiquantitative description of the 110/200 intensity variation across a single fiber measured by a 2 μm X-ray beam.[16]

Monte Carlo Simulations. Analytical models can in principle be extended to complex materials as shown for a mixture of random and oriented phases in carbon fibers.[34] Such models become, however, more difficult to develop as materials become more complex in particular for skin/core differentiation. In the current article, we will therefore explore the more flexible Monte Carlo (MC) approach.[35,36]

For the MC modeling, $N_0 = 10^4$ points are randomly selected within the part of the fiber hit by a $B = 200$ nm beam during a step scan with 200 nm steps. The center of the beam in the x direction is regarded as the nominal position of the beam and is designated with x_p. At every beam position x_p the scattering probability according to a specific rotational disorder model is evaluated. Specifically let (x_j,y_j) be a point selected within the illuminated sample area $A'(x_p)$ (dotted area in Figure 4). The aim is to calculate the Bragg scattered intensity at each position x_p of the beam, which implies evaluation of the following integral

$$I(x_p) = \int_{A'(x_p)} I'(x, y)\,\mathrm{d}A = 2\int_{x_1}^{x_2}\int_{y_1}^{y_2} I'(x, y)\,\mathrm{d}y\,\mathrm{d}x \tag{3}$$

where

$$y_{1,2} = \sqrt{r^2 - x_{1,2}^2} \tag{4}$$

The factor 2 stems from the cylindrical symmetry of the fiber. $I'(x,y)$ is the Bragg scattered intensity from an infinitely small volume element (crystalline domain). For $x_{1,2}$ one has to distinguish four cases (limited for simplicity to $x_p \le 0$):

$$\text{(a) } x_p + B/2 \le -r \Rightarrow \mathrm{I}(x_p) = 0 \tag{5}$$

$$\text{(b) } x_p \le -r \le x_p + B/2 \Rightarrow x_1 = -r,\ x_2 = x_p + B/2 \tag{6}$$

$$\text{(c) } x_p - B/2 \le -r \le x_p \Rightarrow x_1 = -r,\ x_2 = x_p + B/2 \tag{7}$$

$$\text{(d) } -r \le x_p - B/2 < x_p + B/2 \le r \Rightarrow x_{1,2} = x_p \mp \mathrm{B}/2 \tag{8}$$

Similar relations hold for $x_p > 0$. These equations are the mathematical expression of the four possible cases.

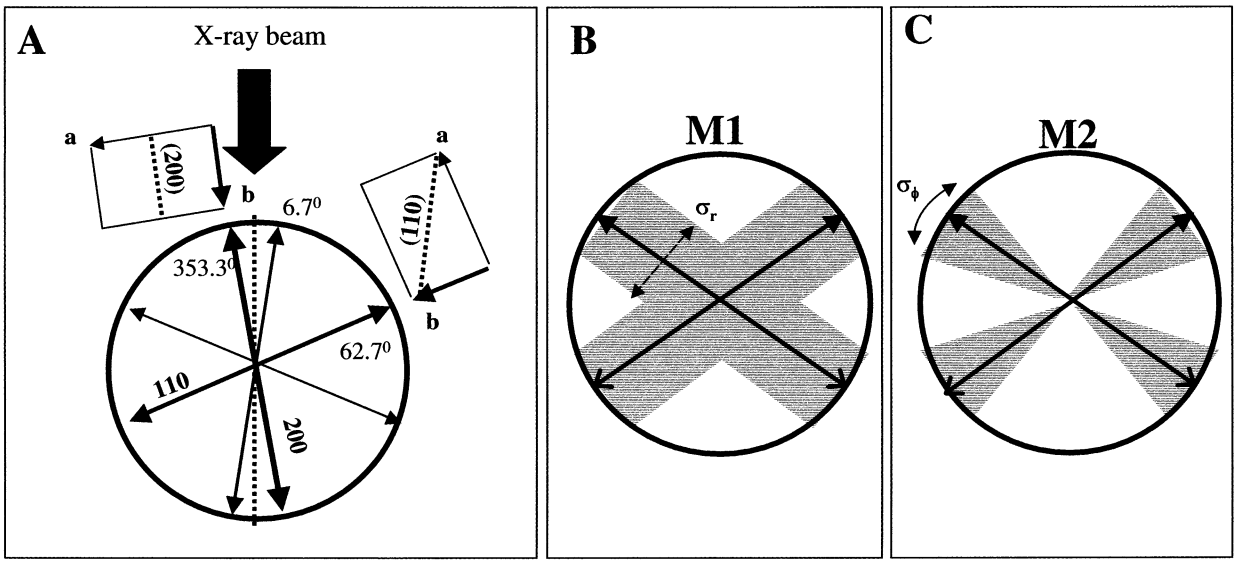

Figure 3. (A) Schematic model showing the Bragg condition for the 110/200 reflections (symbolized by arrows) based on an ideal domain alignment (Figure 2A).[14,16] The clockwise increasing angles of the arrows are defined relative to the direction of the X-ray beam (0°). The orientation of the unit cells corresponding to the scattering from the (110) and (200) lattice planes is shown for the corresponding thicker arrows. The thinner arrows are generated due to the fiber symmetry. (B) Same as for Figure 3A but for a model with a linear increase in rotational domain disorder from skin to core (M1 model). The gray zone indicates the spread of the Bragg condition across the fiber. Solid lines show the ideal Bragg condition for the (110) lattice planes. (C) Same for a correlated rotational domain disorder model with constant rotational angle across fiber radius (M2 model).

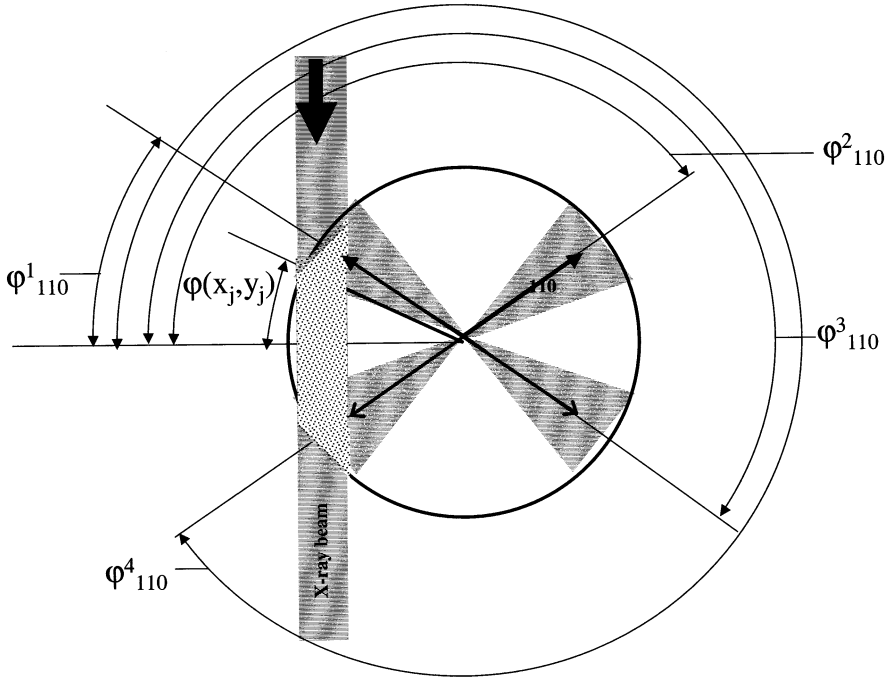

Figure 4. Schematic design of Monte Carlo (MC) simulation for 110 reflection. The points selected for simulations across the illuminated area of the fiber are indicated schematically. $\varphi(x_j,y_j)$ and $\varphi^{1-4}{}_{110}$ denote the angle of the scattering point and of the (110) lattice planes.

The two limiting cases are that the beam does not hit the fiber (case a) or that the beam completely hits the fiber (case d). In cases b and c, the beam partially hits the fiber. Specifically, in case b the beam center x_p is outside ($x_p < -r$) the fiber while in case c the beam center x_p is already inside the fiber ($x_p > -r$).

The integral of eq 3 is evaluated over the illuminated area $A'(x_p)$ of the sample (Figure 4). The MC method hence calculates the integral by approximating the integral of eq 3 with a sum over the intensities $I'(x_j,y_j)$ calculated at each of the $N_0 = 10^4$ points randomly chosen within the area $A'(x_p)$. To do so, $I'(x,y)$ has to be known. Let $p_\varphi(x_j,y_j)$ be the scattering probability for a Bragg reflection at the coordinate (x_j,y_j). The index j denotes the run number of the point randomly chosen ($1 \le j \le N_0$). In the case of an orientational Gaussian distribution of the (110) and (200) lattice planes one can write for the case of model M2 (the corresponding formulas of model M1 are derived at the end of this paragraph)

$$p_\varphi(x_j,y_j) \propto \exp(-(\varphi(x_j,y_j) - \varphi_{110,200})^2/(2\sigma_{110,200}{}^2)) \quad (9)$$

with

$$\varphi(x_j,y_j) = \tan^{-1}(y_j/x_j) \tag{10}$$

being the azimuthal coordinate of the point (x_j,y_j). $\varphi_{110,200}$ is the nominal direction of the four (110) and (200) lattice planes (polar coordinates) (Figure 4). The width of the distribution is taken as $\sigma_{110,200} = 384$ mrad. This value has been adjusted manually using the waveguide data. As the N_0 points are equally distributed via the random choice over the illuminated sample area $A'(x_p)$ and as A' is a function of x_p one has to introduce an appropriate geometric weighting function for the correct counting of each event j:

$$p_A(x_j,y_j) \propto (x_2 - x_1)L(x_j) = 2(x_2 - x_1)\sqrt{r^2 - x_j^2} \tag{11}$$

Hence the final formula for evaluating the Bragg intensity at each beam position s is

$$I(x_p) = I_0 \sum_{j=1}^{N_0} \sum_{\varphi=\varphi^1,\varphi^2,\varphi^3,\varphi^4} p_\varphi(x_j,y_j)p_A(x_j,y_j) \tag{12}$$

The last sum includes the fact that due to the Gaussian orientational disorder the scattering center at (x_j,y_j) can be attributed to one of the four (110) and (200) lattice planes at angles $(\varphi^1, \varphi^2, \varphi^3, \varphi^4)_{110,200}$ (see Figure 3A and Figure 4). In eq 12, I_0 is a parameter in which the structure factor is lumped and which normalizes the maximum of $I(x_p)$ to 1.

We now derive the scattering probability for model M1 by assuming a Gaussian probability distribution for the scattering probability. As can be deduced from Figure 3B, model M1 implies σ_r = constant. The variable determining the scattering probability is the geometric distance $\Delta r_\perp$ to the arrows representing the nominal direction for the (110) and (200) lattice planes. With x_j and y_j being the Cartesian coordinates of the point randomly chosen, this distance $\Delta r_\perp$ reads

$$\Delta r_\perp = \sqrt{(x_j^2 + y_j^2)}\,\sin[\varphi(x_j,y_j) - \varphi_{110,200}] \tag{13}$$

Using a Gaussian probability distribution with width σ_r we finally arrive at

$$p_\varphi(x_j,y_j) \propto \exp\left(-\frac{\Delta r_\perp^2}{2\sigma_r^2}\right) = \exp\left(-\frac{x_j^2 + y_j^2}{2\sigma_r^2}\sin^2[\varphi(x_j,y_j) - \varphi_{110,200}]\right) \tag{14}$$

Simulations of the M1/M2 models assuming the Gaussian approach introduced above are shown in Figure 5. More complicated rotational disorder models can easily be introduced. Thus, the gradient of rotational disorder of the M2 model could vary exponentially. These models will, however, not be discussed as the sensitivity of the simulation method based on two reflections (110/200) was found to be insufficient. While Kevlar has only two strong and well separated equatorial reflections, a larger number of reflections, as found for BPO,[37] might allow more detailed simulations.

The influence of the beam size on the shape of the 110-intensity distribution for the M2 model is shown in Figure 6. The simulations suggest that profile distortions are only negligible for beam sizes ≤0.5 μm.

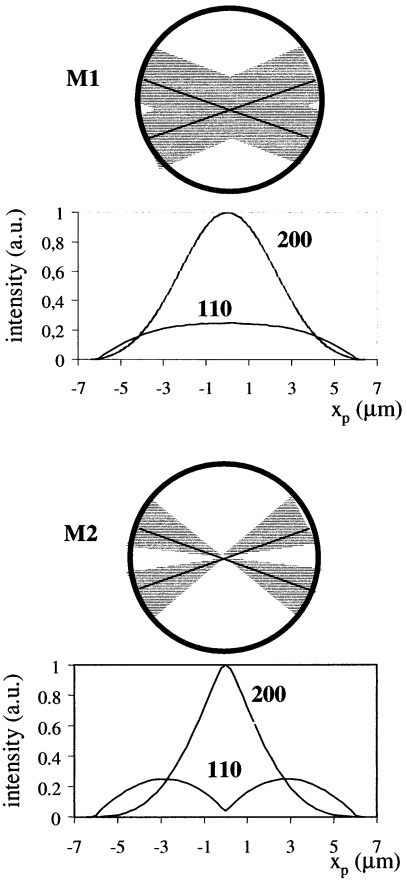

Figure 5. Intensity variation of M1 and M2 models determined by MC-simulations. The M2 model has a linear gradient in σ_r (see text) from the skin to the core. Simulations are based on a 0.2 μm beam and 0.2 μm step resolution.

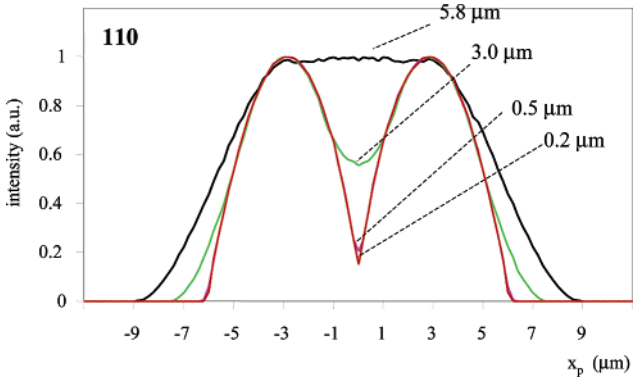

Figure 6. Simulation of 110-intensity of the M2 model across a fiber for selected beam sizes.

Results and Discussions

Particle Size. To compare the waveguide results with other experiments, we first determined the variation in apparent particle size normal to the fiber axis according to the Scherrer[38] equation from the 110/200 reflections. A detailed analysis of particle sizes in Kevlar fiber sections by selected area electron diffraction (SAED) and dark field images of the 110/200 reflections has already been reported.[27] For the series Kevlar[29] → Kevlar[49] → Kevlar[149], we observe a differentiation of particle size along [110] and [100] and the appearance of a gradient starting with Kevlar[49] (Figure 7A). The

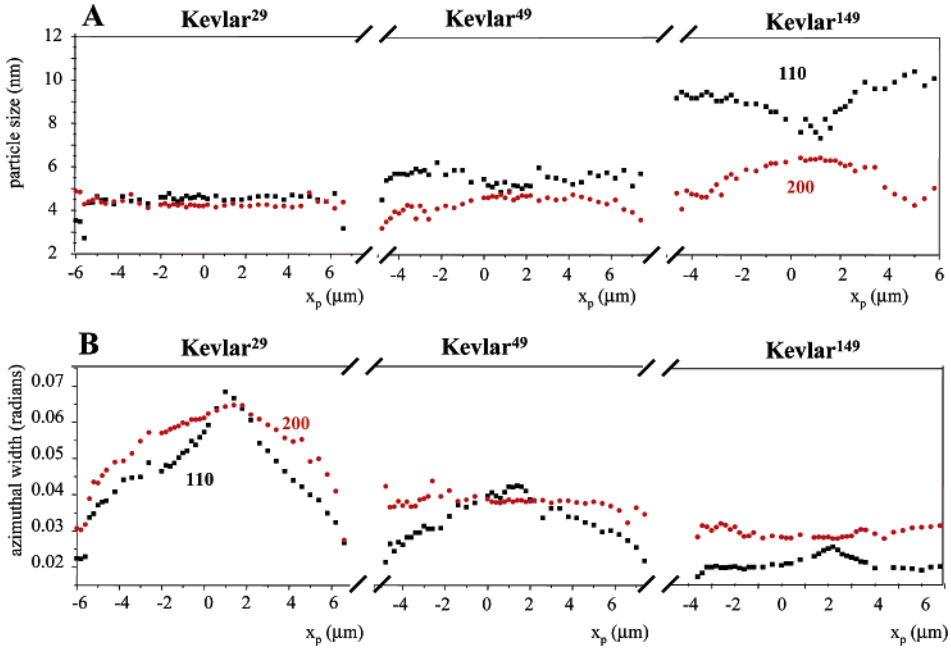

Figure 7. (A) Variation of apparent particle size for the 110/200 reflections in the series Kevlar[29] → Kevlar[49] → Kevlar.[149] (B) Same for variation of azimuthal width.

overall particle size variation has been assigned to preferential growth along the hydrogen-bonded direction (*b* axis),[27] which suggests an increasing correlation of domains along this axis. The differentiation of particle size observed in the present study provides a direct explanation for the increase in size weighted distributions from Kevlar[49] to Kevlar[149] found by SAED.[27] The data suggest that the crystallites are smaller along [100] in a skin layer of about 1 μm thickness, while the particle size along [110] is unaffected by this skin layer.

Orientation Distribution along Fiber Axis. Figure 7B shows the variation of azimuthal width of the 110/200 reflections for the Kevlar fibers. The gradient in azimuthal width observed for Kevlar[29] agrees to the previous data obtained with a 3 μm beam[15] although the higher spatial resolution of the present study shows that the gradient is less smooth. In particular the 110 reflection of Kevlar[29] shows a strong increase in azimuthal width at the core suggesting more axial disorder. The azimuthal width of both reflections decreases in the series Kevlar[29] → Kevlar[49] → Kevlar.[149] The gradient in azimuthal width of the 200 reflection already flattens out for Kevlar,[49] which could reflect a preferential formation of larger fibrils with tie-bundles interconnections along [100], i.e., normal to the radial hydrogen-bonded interconnections.[4] The azimuthal width distribution of 110-planes becomes lower than the angular spread of (200) planes in Kevlar.[149] This could be due to the radial hydrogen-bonded network, resulting in preferential growth along [010] during processing.[27] The larger crystalline domains would result in a smaller angular disorder due to loss of rotational freedom (see Figure 8). Models involving preferential orientation along slip-planes can, however, not be excluded.

Intensity Distribution Simulations. As shown in Figure 6 one should be able to observe a reduction of the 110-intensity according to the M2 model in the center of a Kevlar[49] fiber for a 3 μm beam. The fact that this has not been observed[16] could be due to (i) a M1-type texture as originally assumed or (ii) the presence of disorder which masks the central intensity dip. We

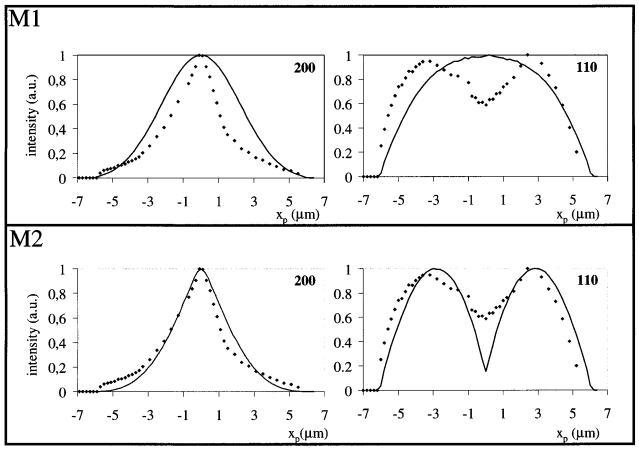

Figure 8. Calculated and observed (Kevlar[149]) 110/200 intensity variation across fiber for M1 and M2 models.

will therefore initially consider Kevlar,[149] which shows the highest lattice perfection.[39]

The simulated and observed variation of relative integral intensities of 110/200 reflections for the M1 and M2 models across the Kevlar[149] fiber are shown in Figure 8. A σ_ϕ value of 385 mrad allowed a better fit of the model to the experimental data than with the experimentally determined value of 420 mrad. This could be due to a small alignment error of the fiber during the σ_ϕ determination or of the fiber used during the scanning experiment. The 110-intensity variation clearly matches better the M2 model although the observed intensity decrease is less important at the center than the calculated. This suggests more a complex model involving skin/core differentiation.

Simulations of a two-layer skin/core model are shown in Figure 9. The skin layer is assumed to be rotationally more disordered than the core layer. This is a reasonable assumption based on TEM results.[4] For simplicity a M1 skin layer and a M2 core are assumed. By varying the radius of the core, one can optimize either the 200 profile (A) or the 110 profile (B). It was, however, not possible

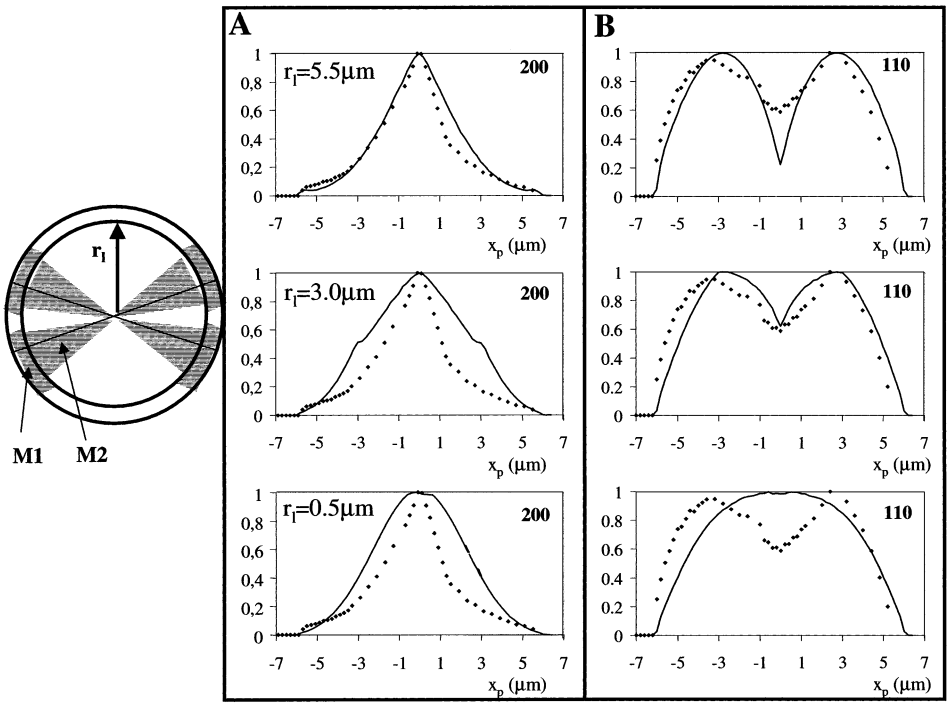

Figure 9. Two-layer (skin/core) model. The skin is assumed to be of M1-type while the core is of M2-type. The radius r_1 of the M2-core has been varied to match either the 200 (A) or the 110 profiles (B).

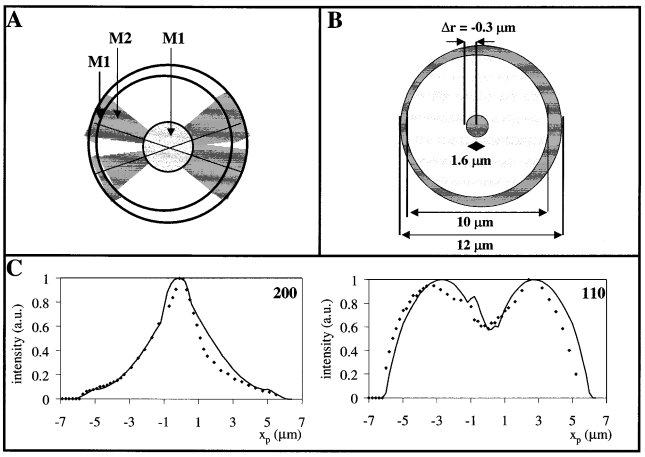

Figure 10. (A) Three-layer model corresponding to the model showed in Figure 9 with an additional central M1-type core. (B) Dimensions of layers corresponding to the best fit. The position of the center of the model with respect to the center of the experimental curve is displaced by 0.3 μm. (C) Observed and simulated 110/200 intensity variation across Kevlar[149] fiber.

to optimize the 110- and 200-intensity profiles for the same r_1 value with a smooth function.

The model can be improved by incorporating a disordered core with M1-type rotational disorder (Figure 10A). One also has to assume that the center of the three layers is shifted by about 0.3 μm from the geometric center of the fiber (Figure 10B). The best agreement between experimental data and simulations is obtained for a 1 μm thick skin layer and a core of 1.6 μm diameter (Figure 10C). The thickness of the skin layer is consistent with the variation of the particle size across the fiber (see above) and with near field microscopy results.[9,31] The observation of 110/200 reflections across the whole fiber diameter of about 12 μm (see above) suggests that this layer is the outermost layer of the fiber, which contrasts with the concept of a purely amorphous skin layer. Data supporting this concept are, however, based on fracture topography[6] or nanomechanical properties[31] which do not provide direct information on the crystallinity.

Table 1. Summary of Fit Parameters for the Three-Layer Model[a]

	core diam (μm)	r_1 (μm)	Δr (μm)	x (%)
Kevlar[29]	1.6	1.8	0	40
Kevlar[49]	1.6	3.8	0	20
Kevlar[149]	1.6	5.0	−0.3	0

[a] r_1 is defined in Figure 9 and the shift of the core (Δr) in Figure 10B. x is the volume fraction of the random phase.

According to our current model the M1-type skin has an angular variance close to that of the M2-type layer. This is, however, different from the M1-type core, as the angular variance of M1 increases toward the fiber center and σ_ϕ stays constant for the M2 model. Hence the disorder (described by the angular variance) is highest in the core (1.9 rad at the core outer radius) and then stays constant at 385 mrad in the M2-type layer but increases and finally increases slightly in the skin layer (460 mrad at r_1). The corresponding changes in the intensity profile are hence necessarily small near the outer fiber radius (see Figures 8−10). Our simple model using these values (see also Table 1) provides a good agreement with the data.

The usefulness of the three-layer model is even more apparent for the Kevlar[29,49] data. To apply the model to these fibers the volume fractions of the three layers have to be modified as shown in Figure 11. The simulations suggest that the more disordered skin layer grows while the intermediate M2 layer decreases from Kevlar[49] to Kevlar[29]. This does apparently not affect the central core.

The fit is, however, not completely satisfying for the skin layer as the observed intensity distribution is higher than the calculated. The only way to get a better agreement was obtained by adding a volume fraction

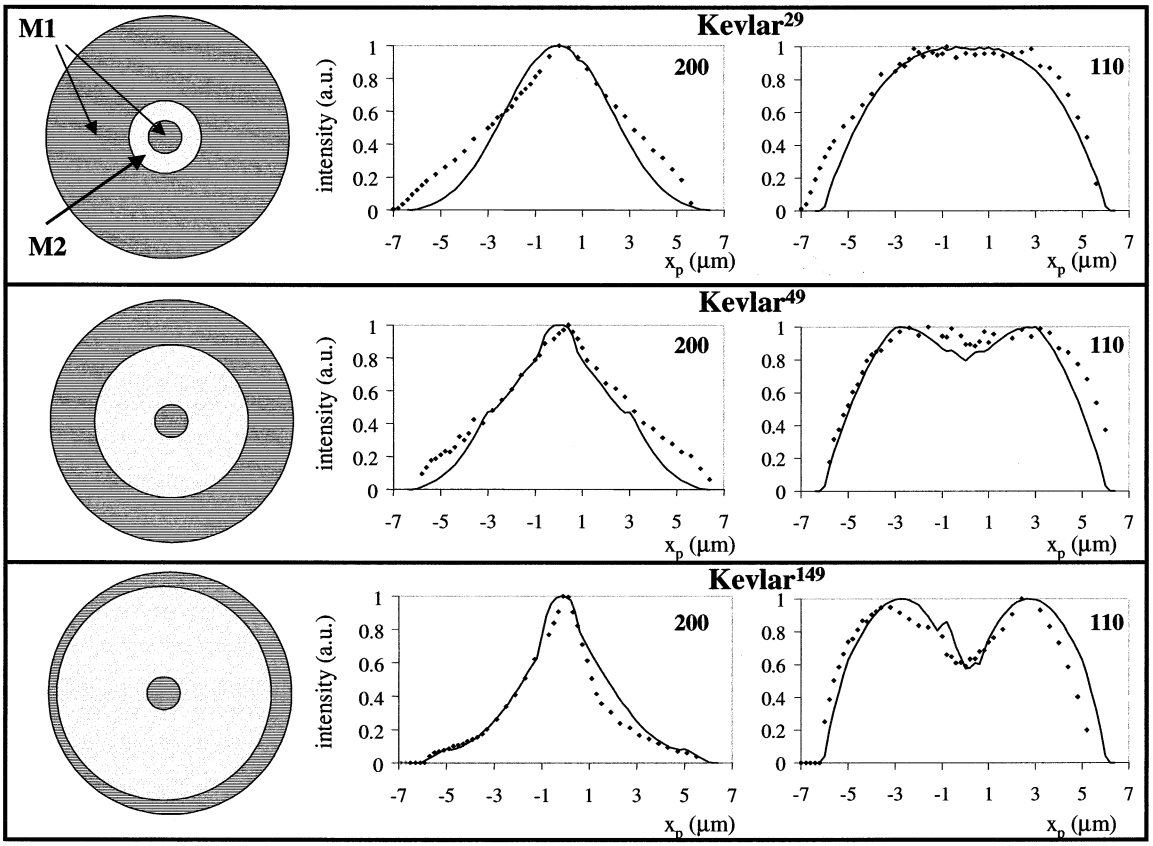

Figure 11. Three-layer model applied to Kevlar[29] and Kevlar.[49] The dimensions of the three layers are shown on the left side. Observed and simulated curves are shown on the right side. Kevlar[149] is shown for comparison.

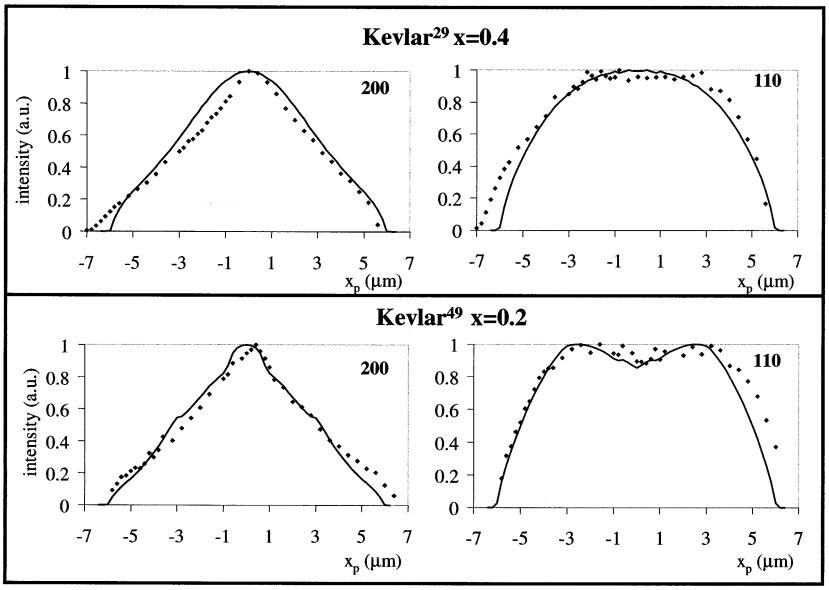

Figure 12. Same as Figure 11 but with an additional random phase (Figure 2B). *x* corresponds to the volume fraction of the random phase.

of a randomly ordered phase (Figure 2B), which was discarded originally (see above) (Figure 12). A summary of the fit parameters is listed in Table 1.

Conclusions

X-ray scanning diffractometry has been extended to an about 100 nm beam. There is no principal technical limitation in a further reduction of X-ray beam size and for a more symmetric spot at a third generation SR source.[40,41] The reduction of spot size will be rather limited by the achievable flux density and the loss of structural information on a specific polymer due to radiation damage.

The Monte Carlo method has been shown to be alternative to analytical simulations for the description of intensity profiles obtained in scanning μ-XRD experiments. The advantage of the MC method is that the extension to complex models and their calculation involving, e.g., skin/core regions can more easily be performed than analytical approaches.

The current simulations for Kevlar, which are based on two equatorial reflections, are necessarily crude and are limited to projection geometry. The data suggest nevertheless the presence of two fractions, which differ in rotational disorder of domains and are spatially separated. The sharpness of the boundary between these fractions is not addressed in the current study but is probably accessible to complementary TEM work.

The large M2 fraction in Kevlar[149] appears to reflect restrictions in domain rotation due to domain size increase resulting in a stronger domain interaction, which could be mediated through tie bundles. The skin and central core has been modeled by the M1 model with a gradient in rotational disorder. Although the M1 model fits the experimental data quite well it is necessarily an idealization, as various disorder gradients (Figure 5) cannot be distinguished. The assumption of a further fraction with random rotational disorder for Kevlar[29] and Kevlar[49] points to a possible highly disordered phase formed at the onset of coagulation. More detailed information on the onset of ordering might be obtained from an in situ study of the coagulation process.

Acknowledgment. We wish to acknowledge useful discussions with P. Engström (Göteborg, Sweden), W. Jark (Trieste, Italy) and S. Lagomarsino (Rome, Italy). The waveguide has been developed at the Budker Institute of Nuclear Physics (Novosibirsk, Russia) in the context of a collaboration with Sincrotrone Trieste (contact: S. DiFonzo-Jark). I. Snigerava (ESRF) provided the SEM of Figure 1.

References and Notes

(1) Kwolek, S. L.; Morgan, P. W.; Schaefgen, J. R.; Gulrich, L. W. *Macromolecules* **1977**, *10*, 1390−1396.
(2) Jiang, H.; Adams, W. W.; Eby, R. K. In *Materials Science and Technology*; Cahn, R. W., Haasen, P., Kramer, E. J., Eds.; VCH: Weinheim, Germany, 1993; Vol. 12, pp 597−652.
(3) Northolt, M. G., Sikkema, D. J., Eds. *Lyotropic Main Chain Liquid Crystal Polymers*; Springer-Verlag: Berlin, 1991; Vol. 98.
(4) Panar, M.; Avakian, P.; Blume, R. C.; Gardner, K. H.; Gierke, T. D.; Yang, H. H. *J. Polym. Sci.: Polym. Phys. Ed.* **1983**, *21*, 1955−1969.
(5) Li, L. S.; Allard, L. F.; Bigelow, W. C. *J. Macromol. Sci. Phys.* **1983**, *B22*, 269−290.
(6) Morgan, R. J.; Pruneda, C. O.; Steele, W. J. *J. Polym. Sci.: Polym. Phys. Ed.* **1983**, *21*, 1757−1783.
(7) Horio, M.; Kaneda, T.; Ishikawa, S.; Shimamura, K. *Sen-i Gakkaishi* **1984**, *40*, T-285-T-290.
(8) Taylor, J. E.; Romo-Uribe, A.; Libera, M. R. *Polymer* **2002**, *43*, 1641−1648.
(9) Li, S. F. Y.; McGhie, A. J.; Tang, S. L. *Polymer* **1993**, *34*, 4573−4575.
(10) Rebouillat, S.; Donnet, J. B.; Wang, T. K. *Polymer* **1997**, *38*, 2245−2249.
(11) Li, S. F. Y. M. A. J.; Tang, S. L. *JVST A* **1994**, *12*, 1891−1894.
(12) Snetivy, D.; Vansco, G. J.; Rutledge, G. C. *Macromolecules* **1992**, *25*, 7037−7042.
(13) Sawyer, L. C.; Chen, R. T.; Jamieson, M. G.; Musselman, I. H.; Russell, P. E. *J. Mater. Sci.* **1993**, *28*, 225−238.
(14) Riekel, C.; Cedola, A.; Heidelbach, F.; Wagner, K. *Macromolecules* **1997**, *30*, 1033−1037.
(15) Riekel, C.; Dieing, T.; Engström, P.; Vincze, L.; Martin, C.; Mahendrasingam, A. *Macromolecules* **1999**, *32*, 7859−7865.
(16) Riekel, C. *Rep. Prog. Phys.* **2000**, *63*, 233−262.
(17) Dobb, M. G.; Johnson, D. J.; Saville, B. P. *J. Polym. Sci., Polym. Symp.* **1977**, *58*, 237−249.
(18) Dobb, M. G.; Johnson, D. J.; Saville, B. P. *J. Polym. Sci., Polym. Phys. Ed.* **1977**, *15*, 2201−2211.
(19) Ade, H.; Smith, A. P.; Cameron, S.; Cieslinski, R.; Mitchel, G.; Hsiao, B.; Rightor, E. *Polymer* **1995**, *36*, 1843−1848.
(20) Smith, A. P.; Ade, H. *Appl. Phys. Lett.* **1996**, *69*, 3833−3835.
(21) Jark, W.; DiFonzo, S.; Lagomarsino, S.; Cedola, A.; Fabrizio, E. D.; Bram, A.; Riekel, C. *J. Appl. Phys.* **1996**, *80*, 4831−4836.
(22) Müller, M.; Burghammer, M.; Flot, D.; Riekel, C.; Morawe, C.; Murphy, B.; Cedola, A. *J. Appl. Crystallogr.* **2000**, *33*, 1231−1240.
(23) Lagomarsino, S.; Cedola, A.; Cloetens, P.; Fonzo, S. D.; Jark, W.; Soullié, G.; Riekel, C. *Appl. Phys. Lett.* **1997**, *71*, 2557−2559.
(24) Blanton, T. N.; Huang, T. C.; Toraya, H.; Hubbard, C. R.; Robie, S. B.; Louer, D.; Goebel, H. E.; Will, G.; Gilles, R.; Raftery, T. *Powder Diffr.* **1995**, *10*, 91−95.
(25) Hammersley, A. "Internal Report ESRF97 HA02T"; ESRF: Grenoble, France, 1997.
(26) Northolt, M. G.; Van Aartsen, J. J. *J. Polym. Sci., Lett. Ed.* **1973**, *11*, 333.
(27) Jackson, C. L.; Schadt, R. J.; Gardner, K. H.; Chase, D. B.; Allen, S. R.; Gabara, V.; English, A. D. *Polymer* **1994**, *35*, 1123−1131.
(28) Grubb, D. T.; Prasad, K.; Adams, W. W. *Polymer* **1991**, *32*, 1167−1172.
(29) Northolt, M. G. *Eur. Polym. J.* **1974**, *10*, 799−804.
(30) Ade, H.; Toledo-Crow, R.; Vaez-Iravani, M.; Spontak, R. J. *Langmuir* **1996**, *12*, 231−234.
(31) Graham, J. F.; McCague, V.; Warren, O. L.; Norton, P. R. *Polym. Commun.* **2000**, *41*, 4761−4764.
(32) Klug, H. P.; Alexander, L. E. *X-ray diffraction procedures for polycrystalline and amorphous materials*, 2nd ed.; Wiley-Interscience: New York, 1974.
(33) Riekel, C. Unpublished material.
(34) Paris, O.; Loidl, D.; Müller, M.; Lichtenegger, H.; Peterlik, H. *J. Appl. Crystallogr.* **2001**, *34*, 473−479.
(35) Bischoff, F. G.; Yeater, M. L.; Moore, W. E. *Nucl. Sci. Eng.* **1972**, *48*, 266.
(36) Roth, S. Ph.D. Thesis, TU Munich: Munich, Germany, 2001.
(37) Davies, R. J.; Montes-Moran, M. A.; Riekel, C.; Young, R. J. *J. Mater. Sci.* **2001**, *36*, 3079−3087.
(38) Warren, B. E. *X-ray diffraction*; Dover Publications Inc.: New York, 1990.
(39) Wu, T. M.; Blackwell, J. *Macromolecules* **1996**, *29*, 5621−5627.
(40) Pfeiffer, F.; David, C.; Burghammer, M.; Riekel, C.; Salditt, T. *Science* **2002**, *297*, 230−234.
(41) *X-ray Micro- and Nano-Focusing: Applications and Techniques II*; McNulty, I., Ed.; SPIE Proceedings 4499; SPIE: Bellingham, WA, 2001.

MA021514G